Journal of Materials Chemistry A

ROYAL SOCIETY OF CHEMISTRY

PAPER

View Article Online
View Journal | View Issue

Cite this: J. Mater. Chem. A, 2023, 11, 24321

3D-printed palladium/activated carbon-based catalysts for the dehydrogenation of formic acid as a hydrogen carrier†

Irene Diaz-Herrezuelo, [a] Gonzalo Vega, *[b] Marina Navarro,[b] Pilar Miranzo, [a] M. Isabel Osendi, [a] Jose A. Casas, [b] Asuncion Quintanilla [b] and Manuel Belmonte *[a]

The development of structured catalyst supports to promote chemical process intensification is of great interest, and porous activated carbon (AC) is an excellent material to overcome this challenge. In addition, the current increasing hydrogen demand and its limitations in terms of transportation and storage require the development of novel approaches for the application of hydrogen. In this study, highly porous and robust 3D-printed patterned AC-based architectures were additive manufactured using the direct ink writing technology. Different AC inks containing a boehmite gel with no organic additives were rheologically characterized to select the most suitable ink for building AC supports, which were thermally treated to promote solid–solid contacts and increase their robustness (strength of ~0.5 MPa) while maintaining a high porosity (86%). Subsequently, the AC supports were impregnated with a 5 wt% palladium (Pd) precursor to develop a 3D Pd/AC catalyst, which could generate hydrogen *via* the dehydrogenation of formic acid (FA), a very promising liquid organic hydrogen carrier, in a fixed-bed reactor. These 3D catalysts produced CO-free hydrogen from FA under ambient conditions with an FA conversion of 81% and hydrogen flow rate of 6 mL min^{-1}. Furthermore, the long-term experiments in continuous mode operation showcased their good catalytic stability and recyclability. These results demonstrate that 3D Pd/AC catalysts exhibit a great potential to develop a new technology using FA as hydrogen carrier.

Received 18th September 2023
Accepted 20th October 2023

DOI: 10.1039/d3ta05644a

rsc.li/materials-a

Introduction

3D printing technologies have rapidly been developed in the chemical industry due to the manufacturing of more efficient and sustainable cellular-structured materials able to enhance process intensification.[1] Also, these technologies are attractive for the construction of scaffolds based on 3D-printed porous activated carbon (AC), which is widely used due to its outstanding physical–chemical properties as an adsorbent[2] and catalyst support.[3]

At present, two main approaches have been proposed for additive manufacturing 3D cellular AC monoliths. The first approach employs organic matter as the feedstock for printing the scaffold. For instance, they can be built by stereolitography (SLA) using photoresins,[4,5] or can be printed by direct ink writing (DIW) employing as feedstock a resorcinol and formaldehyde solution[6] or whey.[7] Subsequently, the printed part is subjected to pyrolysis or carbonization step followed by CO_2 activation. The other approach involves the direct use of a commercial AC powder to prepare an aqueous AC-based ink with a particular rheology, which is then printed by DIW (also known as robocasting).

The latter procedure offers significant benefits over the carbonization/activation process, such as a reduction in post-printing steps and in contaminants and/or residues. Besides, considering that the yield of AC formation *via* the polymeric route is sometimes limited,[5] employing pristine AC, which retains its physical and chemical properties, is also advantageous. However, carbon materials are commonly hydrophobic, which makes it extremely difficult to achieve a successful printed structure using water as the liquid medium in the ink if the powder is not pre-functionalized. Alternatively, AC powder can be mixed with a supporting material (mainly zeolite) and/or a binder.

To date, some works have reported the manufacturing of 3D cellular AC-based structures by DIW, mainly for CO_2 adsorption related applications.[8–13] For example, Regufe *et al.*[8] first claimed the preparation of 3D scaffolds with 70 wt% of zeolite and 30 wt% of AC printed with an ink that contained a carboxymethylcellulose (CMC) binder. Recently, the same group[9]

[a]Instituto de Cerámica y Vidrio (ICV), CSIC, Kelsen 5, 28049 Madrid, Spain. E-mail: mbelmonte@icv.csic.es

[b]Chemical Engineering Department, Universidad Autónoma de Madrid, 28049, Madrid, Spain. E-mail: gonzalovm95@gmail.com

† Electronic supplementary information (ESI) available. See DOI: https://doi.org/10.1039/d3ta05644a

increased the AC content of the ink to 47.5 wt% (plus 47.5 wt% of zeolite and 5 wt% of CMC), obtaining a high CO_2 adsorption capacity and selectivity. In both studies, the binder was not thermally removed to avoid potential damage to AC. Mendes *et al.*[10] investigated the CO_2 adsorption capacity of two distinct 3D cellular AC-based structures obtained from a mixture of zeolite/AC/bentonite (as binder) with compositions (wt%) of 45/45/10 and 0/90/10, and porosities in the range of 56% to 62%, respectively, after a thermal treatment at 550 °C in nitrogen (N_2). The results confirmed the better adsorption performance of the monoliths containing zeolite. Verougstraete *et al.*[11] also reported the printing of 3D AC structures for CO_2 capture from biogas using a mixture of 50 wt% AC and 50 wt% potassium silicate, which acted as binder and enhanced the capture of CO_2 by forming potassium carbonate. Rangel-Sequeda *et al.*[12] developed AC scaffolds from AC : CMC ink with a mass ratio of 1 : 2 by heating the as-printed material to 600 °C to burn off the CMC. The monoliths exhibited similar CO_2 adsorption capacity to their powder precursors. Finally, Acuña-Bedoya *et al.*[13] also employed CMC to produce printable AC inks, with an AC : CMC weight ratio of 32 : 68. The scaffolds were heat-treated at 600 °C and employed as electrodes in an adsorption-electro-oxidation system to degrade non-steroidal anti-inflammatory drugs.

To date, the use of 3D-printed cellular AC structures in heterogeneous catalysis has not been investigated, and thus the goal of the present work was, firstly, to manufacture highly porous and robust 3D-printed patterned AC-based architectures, and secondly, use them as catalyst supports in hydrogen production, which is a topic of great interest due to the expected exponential increase in hydrogen demand over the next two decades.

Nevertheless, the low density and flammability of hydrogen make its transportation and storage difficult and risky,[14,15] and the current technologies employed for hydrogen storage are expensive given that they require either high-pressure compression in cylinders or liquefaction in cryogenic tanks.[16–18] Thus, to overcome these issues, liquid organic hydrogen carriers (LOCHs) have emerged as a promising solution,[14,17,19,20] considering that they can be transported under ambient conditions utilizing the existing infrastructure designed for gas and crude oil transportation. These carriers store hydrogen through catalytic hydrogenation/dehydrogenation reactions, allowing the efficient and reversible release of hydrogen as needed. Recently, formic acid (FA) has gained attention as a viable LOHC because its production can be based on emerging technologies linked to the carbon dioxide (CO_2) capture and use, facilitating a more sustainable approach for the distribution of hydrogen.[21–23] Moreover, the catalytic dehydrogenation of FA into hydrogen (H_2) and CO_2 can be performed with high efficiencies under low temperature operating conditions, below 60 °C, without the formation of any undesirable by-products.[24,25] Among the catalysts studied for the dehydrogenation of FA, palladium (Pd) nanoparticles supported on AC powder exhibit enhanced catalytic activity because AC promotes the synthesis of Pd nanoparticles with small sizes and high Pd^{2+}/Pd^0 ratios.[26–31] However, to the best of our knowledge, structured Pd/AC catalysts for scaling up the dehydrogenation of FA have not been developed. Structured reactors are known for their high and straightforward scalability. The size of the structured catalyst in the reactor can be adjusted to the reactor size without affecting its catalytic performance once its internal structure is preserved. Maintaining the same internal structure ensures the same available surface area, thereby preventing hydrodynamics and mass transfer from influencing the catalytic performance on a large scale. Therefore, in this work, we explored the manufacturing of 3D Pd/AC catalysts *via* the Pd impregnation of 3D-printed AC supports for the catalytic dehydrogenation of FA as a hydrogen carrier. The final goal is to facilitate the on-demand production of hydrogen under near ambient conditions.

In this study, different AC inks containing a boehmite gel were rheologically characterized to identify the most appropriate ink to manufacture AC scaffolds by DIW. Prior studies confirmed the benefits of using a boehmite gel to enhance the printability of ceramic inks.[32] Although other inorganic gels could be employed, boehmite can increase the mechanical and chemical resistance of the printed scaffolds once thermally transformed into Al_2O_3, which is of great interest considering the demanding conditions of catalytic reactors.

Experimental

Additive manufacturing of AC-based supports

AC powder (<100 nm particle size, Merck) was selected for the preparation of 3D catalytic supports and characterized by different techniques. The specific surface area (S_{BET}) and external surface area (A_{EXT}) were measured using the Brunauer–Emmett–Teller method (BET) and a TriStar 3000 instrument (Micrometrics) at a degassing temperature of 120 °C in nitrogen. Carbon, sulphur, nitrogen, and oxygen contents were determined using different elemental analyzers, *i.e.*, LECO CS-200 for carbon and sulphur and LECO TC-500 for nitrogen and oxygen. Thermogravimetric/differential thermal analysis (TGA/DTA, Q600, TA Instruments) tests were performed up to 1000 °C at a heating rate of 5 °C min^{-1} in air. The characterization of the AC powder is shown in Table S1 and Fig. S1 (see ESI†), highlighting its high S_{BET} (738 m^2 g^{-1}) and A_{EXT} (514 m^2 g^{-1}) values, and carbon and oxygen contents of 87.6 and 7.3 wt%, respectively. In addition, the AC powder was stable in air up to 450 °C, and then began to decompose, losing weight with an increase in temperature until completely burnt at 600 °C, as evidenced by the TGA/DTA data (Fig. S1†).

A boehmite gel (AlO(OH)) was added in different proportions to the AC powder, and the corresponding AC-based inks were prepared by sequentially mixing Milli-Q water, AC powder and boehmite gel (B), using three distinct AC/B weight ratios of 90/10, 70/30 and 55/45. The inks were homogenized after each addition (water, AC or B) in a planetary centrifugal mixer (AR-250, Thinky Company) at 2000 rpm for 30 s using silicon nitride balls as milling media. The boehmite gel was previously prepared by simultaneously stirring (500 rpm) and sonicating a colloidal dispersion containing 41 wt% of boehmite powder (Dispal 11N7-80, SASOL, 220 nm particle size modified with 0.1 wt% of nitric acid) and Milli-Q water in an ice/water bath for

90 min. The apparent viscosity (η) as a function of the shear rate ($\dot{\gamma}$), and the shear storage (G') and loss (G'') moduli *versus* the shear stress (τ) of the AC-based inks were determined using a rheometer (CVO 100 D, Bohlin Instruments) with a cone-and-plate tool (diameter: 40 mm and cone angle: 4°) at 25 °C in the range of 0.1–100 s^{-1} and 10^1–10^4 Pa, respectively.

Unframed cylindrical 3D cellular structures (16.2 mm in diameter and 7.9 mm in height) formed by 12 successive printed layers, each containing a linear array of 9 parallel filaments in the *X*–*Y* plane and orthogonally assembled with respect to the adjacent layer, were computer-designed with CAD software (RoboCAD 4.2, 3-D Inks LLC). The ink was extruded with a three-axis robocasting system (A3200, 3-D Inks LLC) at a constant speed of 10 mm s^{-1} at room temperature in air on an alumina substrate through a nozzle tip with an inner diameter of 840 μm (Precision Tips; EFD Inc). The as-printed AC/B monoliths were heat-treated at 1300 °C under a vacuum atmosphere in a high-temperature graphite furnace (Thermal Technology Inc), with a holding time of 30 min at the set temperature and heating/cooling rates of 10 °C min^{-1}. The as-printed and heat-treated scaffolds were microstructurally characterized by optical stereomicroscopy (Nikon SMZ1000) and field-emission scanning electron microscopy (FESEM, Hitachi S-4700). In addition, the densities and porosities of the heat-treated scaffolds were fully characterized.[33] In brief, the geometrical density (ρ_{geo}) was calculated from the scaffold weight and dimensions, whereas the bulk density (ρ_{bulk}) and apparent density (ρ_{app}) were assessed by the Archimedes' method. Total porosity (π_{total}) was estimated considering ρ_{geo} and the theoretical density (ρ_{th}) of the scaffold after heat treatment, which was mainly constituted by AC (ρ_{th} = 2.10 g cm^{-3}) and alumina (δ- and θ-Al_2O_3, $\rho_{th} \sim 3.59$ g cm^{-3}), where the latter was the result of the transformation of boehmite into these alumina crystalline phases. The rod porosity (π_{rod}) was determined using ρ_{bulk}, while the porosity of the open channels or 3D porosity (π_{3D}) was calculated using π_{total}, π_{rod} and the volume fraction of rods in the structure. Finally, the total open rod porosity ($\pi_{total\text{-}open\text{-}rod}$) was obtained from the volume fraction of rods and the open rod porosity ($\pi_{open\text{-}rod}$), which was estimated using π_{rod} and ρ_{app}. The crystalline phases were identified by X-ray diffraction (XRD, Bruker D8 Advance) using a Linx Eye detector and CuKα radiation in the 2θ range of 10° to 80°. The S_{BET}, pore size distribution and TGA/DTA analyses of the scaffolds were performed using the same methodology as that previously described for the AC powder.

The top/bottom faces of the 3D structures were gently ground to ensure homogeneous close contact during the mechanical compression tests. At least four monoliths with a diameter of 15.6 mm and height of 7.2 mm were compressive loaded (ZwickiLine Z5.0 TS, Zwick-Roell) using a 5 kN load cell and a displacement rate of 0.5 mm min^{-1}. Compressive strength (σ_c) was calculated considering the maximum compressive stress and the cylindrical contact area of the scaffold.

Preparation and characterization of 3D Pd/AC catalysts

Pd nanoparticles were synthesized on the AC scaffolds *via* the impregnation method, followed by thermal treatment under a reducing atmosphere. The nominal load of Pd was fixed at 5 wt%. In a typical preparation, six AC monoliths (equivalent to 3 g) were submerged in a precursor solution at 65 °C and agitated for 1 h in a rotary and oscillating mixer (Movil-Rod, J.P. Selecta). The precursor solution was prepared by dissolving 0.27 g of $PdCl_2$ (Merck) in 7.5 mL of 0.58 mol L^{-1} of HCl (Panreac). This solution was mixed with 20 mL of Milli-Q water to ensure complete immersion of the monoliths in the Falcon™ tubes used in the mixer. Subsequently, the precursor solution was divided into six aliquots to submerge one monolith in each aliquot. Then, they were placed in an oven at 95 °C until the water was completely evaporated. During the treatment, the monoliths were flipped to promote the even distribution of Pd on the AC scaffold surface. The Pd-impregnated monoliths were washed with Milli-Q water and oven-dried at 60 °C overnight. Finally, they were reduced to remove the residual chlorides in a quartz tube under an H_2/N_2 stream (50/100 N mL min^{-1}) at 250 °C for 2 h at a heating rate of 10 °C min^{-1}. The resulting catalysts were labelled as 3D Pd/AC.

Different techniques were used to characterize the Pd/AC catalysts before ("fresh") and after ("use") the catalytic reaction. In addition to S_{BET} and XRD (Bruker D5000) measurements, SEM (Hitachi S-3000N) with coupled energy dispersive X-ray spectroscopy (EDX, XFlash 6I30, Bruker) and transmission electron microscopy operating at 200 kV (TEM, JEOL 2100F) were employed to visualize the Pd dispersion and measure the Pd particle size (by counting at least 100 features and using the ImageJ software), respectively. High-resolution TEM (HRTEM) images were also recorded at 300 kV (JEOL JEM GRAND ARM300CF) to measure the lattice spacing of the Pd nanoparticles. The Pd content was measured by total reflection X-ray fluorescence (TXRF) using a benchtop S2 PICOFOX TXRF spectrometer (Bruker Nano). The exposed Pd surface species (Pd^0 and $Pd^{\delta+}$) were quantified by X-ray photoelectron spectroscopy (XPS). The spectra were measured with a PHI5000 VersaProbe II using a monochromatic Al-Ka X-ray beam (1486.6 eV). Charge referencing was measured against adventitious carbon (C1s at 284.5 eV). The monoliths were pulverized for all the analyses except for the visualization of the Pd nanoparticle distribution by SEM.

Catalytic dehydrogenation reactions

The FA dehydrogenation reaction was conducted in a fixed-bed reactor operated in continuous mode. Five 3D Pd/AC pieces (catalyst weight, $W_{CAT} \sim 2.5$ g) were settled in a double jacket glass tube (GE Healthcare, XK16/20 mm) between two beds of spherical glass beads of 2 mm diameter to help to the flow distribution. Water, as the heating fluid, was recirculated in the double jacket to ensure the desired reaction temperature inside the reactor, T = 25–55 °C. The FA solution ($C_{FA,0}$ = 0.5–1 M) was preheated and fed to the bottom of the reactor at a liquid flow rate (Q_L) = 0.25 mL min^{-1} by a piston pump (Shimadzu LC-20AD). Thus, the reactor was operated at spatial time (τ) = $W \cdot Q_L^{-1}$ = 160 g_{CAT} h L^{-1}. Helium (He) was used as the carrier gas at flow rate (Q_{He}) = 17 N mL min^{-1} to ensure the continuous flow of gas (Bronkhorst High Tech). The liquid and gas from the reactor effluent were continuously separated and cooled in

a Peltier cell, collected and analyzed. Gas samples were collected using gas sampling bags (Supelco). Long-term experiments were conducted under different operating conditions to study the deactivation of the 3D Pd/AC catalyst and its recyclability in continuous mode operation. After each experiment, the monoliths were removed and dried at 60 °C for 24 h prior to the next use. Additionally, one used monolith was used for characterization and, then, the liquid flow rate was adjusted proportionally to the catalyst mass to maintain the same $\tau = 160$ g_{CAT} h L^{-1}. All experiments were performed at ambient pressure (1 atm).

The evolution of the gas composition during the reaction was studied using a gas chromatograph (Agilent 6890) equipped with a thermal conductivity detector employing a Varian select permanent gases/CO_2 column and He the as carrier gas for the analysis. H_2, CO, CO_2, O_2 and N_2 gases were calibrated employing three commercial standards. Alternatively, the FA concentration (C_{FA}) in the liquid effluent was measured by spectrophotometry at the wavelength of 210 nm in a Cary 60 Vis-UV spectrophotometer. The FA conversion (X_{FA}) and evolve gas flow rate (Q_{GAS}) were used to evaluate the catalytic performance, as follows:

$$X_{FA}(\%) = \frac{C_{FA,0} - C_{FA}}{C_{FA,0}} \times 100 \quad (1)$$

$$Q_{GAS}\ (\text{mL min}^{-1}) = Q_{He}\ (\text{mL min}^{-1}) \times \text{dilution factor} \quad (2)$$

The dilution factor was calculated according to the gas composition measured in the gas effluent. The detailed calculations are provided in the ESI.†

Results and discussion

3D-printed AC-based supports

The rheological characterization of the different AC-based inks is presented in Fig. 1a and b. All the inks exhibited pseudoplastic behavior, with the η values decreasing by about three orders of magnitude as $\dot{\gamma}$ augmented (Fig. 1a). In principle, this response will favor the extrusion of the ink in the syringe through the cylindrical nozzle when pressure is applied by the piston of the robocasting equipment due to the lower ink viscosity at high shear rates, and also maintain the filamentary shape of the printed rods as they leave the nozzle tip (high viscosity at very low shear rate). However, the large AC content of the 90/10 ink did not allow developing a fully homogenous ink, which contained some lumps, leading to a viscosity curve with some fluctuations. Regarding the shear modulus response (Fig. 1b), the 70/30 and 55/45 inks presented prolonged and constant G' data at around 6×10^5 Pa, which were above the G'' curves ($\sim 1 \times 10^5$ Pa) until crossing at the yield stress (τ_y), corresponding to values of 1600 and 1050 Pa, respectively. For both ink compositions, the G' and τ_y data allowed the assembly of self-supported and robust 3D structures by robocasting, where the 70/30 ink resulted in filaments with larger stiffness than those obtained with the 55/45 ink. In contrast, the 90/10 ink presented lower G' values, which quickly decreased with the shear stress, leading to a substantial reduction in τ_y ($\sim$100 Pa) and preventing the construction of a self-supported scaffold.

Table 1 summarizes the composition of the different aqueous AC/B inks. The solid content (AC + B) of all the inks was in the range of 40–42 wt%. Considering the rheological data of the inks, printability of the 3D structures, and catalytic premise that suggests employing supports with the maximum AC content, the 70/30 ink was selected as the most suitable composition for printing the catalytic supports.

Accordingly, the next step was to manufacture the monoliths following the CAD model shown in Fig. 1c to fit the dimensions of the catalytic reactor. The as-printed scaffolds (Fig. 1c and d) fully reproduced the design and no cracks were observed in the 3D structure, showing straight filament arrays in each layer (Fig. 1d). Further thermal treatment at 1300 °C did not damage the scaffolds (Fig. 2a and b) and led to the complete transformation of boehmite into δ- and θ-Al_2O_3 (Fig. 2c). These crystalline phases were chemically resistant to the dehydrogenation reaction of FA, and the monoliths kept their mechanical integrity, as proven by introducing the scaffolds in a beaker containing FA at 55 °C under mechanical stirring for 1 h (see Fig. S2†). After the transformation of boehmite, the composition ratio of the sintered support was recalculated considering the changes in the theoretical density of boehmite (3.03 g·cm^{-3}) and δ- and θ-alumina ($\sim$3.59 g cm^{-3}). The 3D structure was formed by approximately 71.5 wt% AC and 28.5 wt% alumina, which is in good agreement with the TGA/DTA data (Fig. S1†).

The 3D AC/Al_2O_3 structures showed some shrinkage with respect to the CAD model of 8.2% in height and 3.7% in diameter and, therefore, the CAD model was redesigned to achieve the final targeted dimensions (7.9 mm in height and 16.2 mm in diameter). The final width of the open channels was 710 ± 30 μm and the diameter of the rods was 760 ± 20 μm. The 3D structures were lightweight (ρ_{geo} = 0.36 g cm^{-3}), highly porous (π_{total} = 85.8%), with 3D macroporosity (π_{3D}) of 45.6%, total rod porosity (π_{rod}) of 40.1%, and open rod porosity

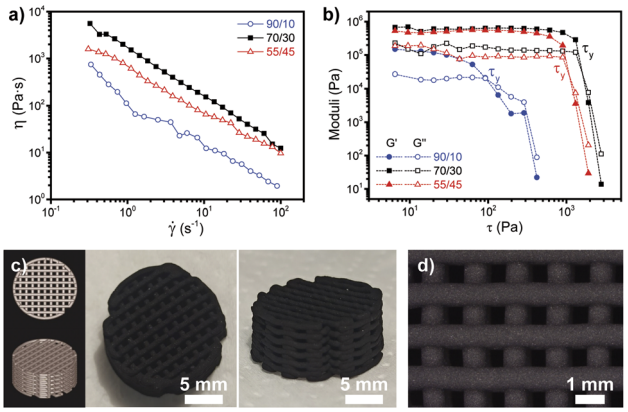

Fig. 1 (a) Apparent viscosity (η) *versus* shear rate ($\dot{\gamma}$) and (b) shear storage (G') and loss (G'') moduli *versus* shear stress (τ) of the different inks. (c) Top and isometric CAD models and optical images of the corresponding as-printed AC/B 70/30 scaffolds. (d) Top view of the as-printed patterned AC/B 70/30 structure.

Table 1 Composition (wt% and vol%) of the distinct aqueous AC/B inks

	AC content		B content			Water content		Solids content	
AC/B label	wt%	vol%	wt%	vol%	AC/B wt. ratio	wt%	vol%	wt%	vol%
90/10	35.9	22.6	4.1	1.7	8.8	60.0	75.7	40.0	24.3
70/30	29.5	19.2	12.5	5.4	2.3	58.0	75.4	42.0	24.6
55/45	22.7	14.9	18.6	8.1	1.2	58.7	77.0	41.3	23.0

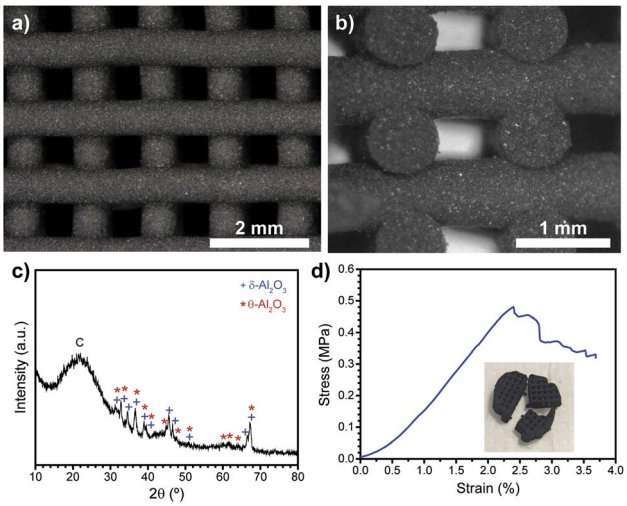

Fig. 2 Characterization of the sintered AC/B 70/30 scaffolds. (a) Top and (b) cross-section views of the 3D structure. (c) XRD pattern showing carbon and δ- and θ-Al_2O_3 peaks. (d) Representative stress–strain curve and image of the scaffold after the compressive test.

($\pi_{total\text{-}open\text{-}rod}$) of 17.2%, considering a theoretical density of 2.55 g cm^{-3} for the sintered 3D AC/B 70/30 structures. Besides, the scaffolds exhibited an S_{BET} of 454 m^2 g^{-1} and A_{EXT} of 329 m^2 g^{-1}, which are very close to the expected values considering the AC content in the 3D structure and the common low S_{BET} and A_{EXT} values attained for high-temperature alumina crystalline phases.[34]

One important parameter to consider in 3D AC/Al_2O_3 supports is their mechanical response, given that they must have sufficient mechanical resistance to be handled and endure the Pd infiltration process, and especially the demanding operating conditions in the catalytic reactor. Fig. 2d shows a representative example of a strain–stress curve for the scaffolds recorded during the compression test, where an initial linear elastic region was clearly observed, which is related to the increasing deformation (bending/buckling) of the AC/Al_2O_3 cells. The apparent elastic modulus (E) of the 3D structures can be assessed from the slope in the linear elastic region in the stress (MPa) *vs.* strain (%) plot, obtaining a value of E of 0.27 ± 0.06 MPa. Once the maximum stress was reached, *i.e.*, the crushing point or compressive strength (σ_c of 0.49 ± 0.04 MPa and strain of 2.35% ± 0.29%), the stress diminished and fracture of the struts occurred, although the scaffold did not catastrophically collapse (see in the inset in Fig. 2d, showing an image of the fractured scaffold). At present, although some studies on the mechanical strength of 3D-printed AC-based materials have been published, only few of them provided the total porosity of the scaffolds, which is an essential parameter affecting their strength. In this case, 3D AC cellular structures manufactured by SLA (from tannin-based resins)[5] and by DIW (from whey)[7] obtained compressive strength values of 1.4 MPa (π_{total} = 83%) and 5.0 MPa (π_{total} = 70%), respectively, and thus, the present 3D AC/Al_2O_3 structures, with a slightly higher porosity (π_{total} = 86%), exhibited a mechanical response in the same range. Other works on robocast AC-based materials achieved strength values ranging from 0.2 to 3.5 MPa,[8,9,12] although their total porosities were not provided.

Fresh 3D Pd/AC catalysts

The physical, chemical, and textural properties of 3D Pd/AC monoliths are summarized in Table 2. The results indicate that the attachment of Pd nanoparticles on the surface of the AC scaffold led to a reduction in the available area, *i.e.*, micro- (S_{BET}) and mesoporous area (A_{EXT}) in the scaffolds, which can be attributed to the deposition of the Pd nanoparticles inside the pores of the 3D structure. The Pd nanoparticles exhibited

Table 2 Main physical, chemical, and textural properties of the 3D AC supports, and fresh and used 3D Pd/AC catalysts. Pd particle size (d_p), specific surface area (S_{BET}), and external surface area (A_{EXT}) are included

Material	Pd (wt%)	Pd^{2+}/Pd^0 (at%)	d_p (nm)	S_{BET} (m^2 g^{-1})	A_{EXT} (m^2 g^{-1})	Carbon (wt%)	Hydrogen (wt%)
3D AC support	—	—	—	454	329	61.2	—
Fresh 3D Pd/AC	4.9	1.4	1.9 ± 0.4	315	155	65.6	0.5
1st use at 55 °C	4.8	0.7	3.8 ± 0.7	360	172	65.6	0.5
3rd use at 55 °C	5.1	0.6	4.4 ± 1.5	413	184	66.2	0.5
5th use at 55 °C	5.1	0.5	4.4 ± 1.0	440	195	67.2	0.5
1st use at 25 °C	4.7	1.4	1.9 ± 0.3	380	171	65.6	0.4
3rd use at 25 °C	4.7	1.1	2.3 ± 0.3	427	185	65.4	0.6
5th use at 25 °C	4.5	0.9	2.8 ± 0.5	389	177	66.6	0.5

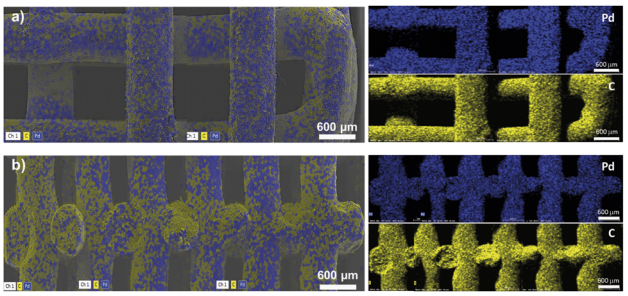

Fig. 3 SEM-EDX mapping for C (yellow color) and Pd (blue color): (a) top and (b) cross-sectional views of fresh 3D Pd/AC catalysts.

a homogeneous surface distribution in both the exposed areas and inner structure, as clearly shown in the SEM-EDX elemental mapping (Fig. 3).

Alternatively, the measured Pd content corresponded to the target value of 5 wt% (Table 2), which confirms the adequacy of the present impregnation method. The Pd particle size (d_P) was 1.9 ± 0.4 nm (Table 2 and Fig. 4a and b). The measured lattice spacing of various Pd nanoparticles was 1.375, 1.945, 2.245, 2.153 and 2.644 Å, which correspond to the lattice spacing of Pd(220), Pd(200), Pd(111), PdO(110) and PdO(101), respectively (Fig. 4c and d).[35] In addition, the XRD patterns (Fig. 5a) showed the characteristic peaks for AC ($2\theta = 24.7°$, 57.3° and 61.8°), δ-Al2O3 ($2\theta = 36.5°$, 38.9°, 45.7°, 66.5° and 67.2°), PdO ($2\theta = 33.8°$ and 43.8°) and Pd^0 ($2\theta = 40.4°$, 46.8° and 68.3°).[36,37] Therefore, the identified Pd crystalline phases agree with that measured by HRTEM. It should be noted that a crystalline PdO phase was observed with a higher amount of under-coordinated PdO surface, such as PdO(101) than PdO(110) surface, which are both desirable species for high catalyst efficiency and selectivity.[38] Besides, the XPS spectrum in the Pd 3d region (Fig. 5b)

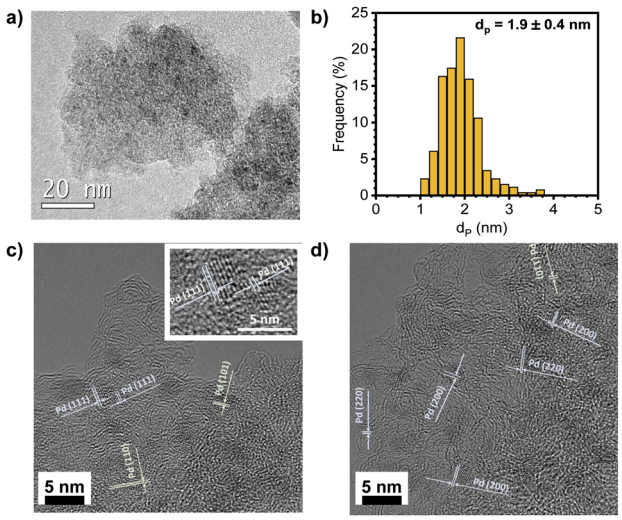

Fig. 4 Representative characterization results of fresh 3D Pd/AC catalysts: (a) TEM image, (b) Pd particle size (d_P) distribution, and (c and d) HRTEM images showing the lattice spacing of Pd and PdO. Inset in (c) corresponds to a high magnification field.

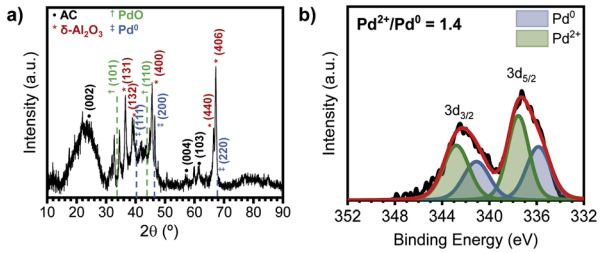

Fig. 5 (a) XRD pattern and (b) XPS spectrum of the Pd 3d core level for fresh 3D Pd/AC catalysts.

exhibited two broad bands associated with the $3d_{5/2}$ and $3d_{3/2}$ transitions.[39] The deconvolution of each band evidenced the existence of two peaks. Specifically, the peaks at 335.9 and 341.1 eV are ascribed to Pd^0, whereas the peaks at 337.6 and 342.8 eV are related to Pd^{2+}, with PdO as the most likely species.[15,26,27,40] The estimated Pd^{2+}/Pd^0 ratio was ~1.4.

Catalytic performance of the 3D Pd/AC catalysts

The results obtained in the FA dehydrogenation experiments under different operating conditions are presented in Fig. 6. The X_{FA}, Q_{GAS} and H_2/CO_2 ratio in the evolved gas were monitored as a function of time-on-stream until the complete loss of activity. The maximum X_{FA} and evolved Q_{GAS} values, time without observing deactivation (t_{stable}), time to achieve total deactivation ($t_{operation}$), total volume of the evolved gas (V_{GAS}, calculated by determining the area under the Q_{GAS} *vs.* time on stream curve until complete deactivation) and total volume of H_2 produced (calculated considering V_{GAS} and the concentration of H_2 in the gas) were obtained from the curves in Fig. 6 and summarized in Table 3. In all cases, no CO was detected in the evolved gas or Pd in the aqueous effluent. Therefore, the 3D Pd/AC catalysts were 100% selective for the dehydrogenation of FA and the deactivation was not caused by Pd leaching.

As can be seen in Fig. 6 and Table 3, the X_{FA} values before starting the progressive deactivation were high, which ranged from 81% to 99%. Both a low $C_{FA,0}$, and especially high temperature are beneficial for the disappearance of FA. This activity is difficult to compare with that of other catalysts due to the different operating conditions used in the FA dehydrogenation conducted in liquid phase and continuous reactors. For instance, the powdered 5 wt% Pd/AC catalyst studied by Caiti

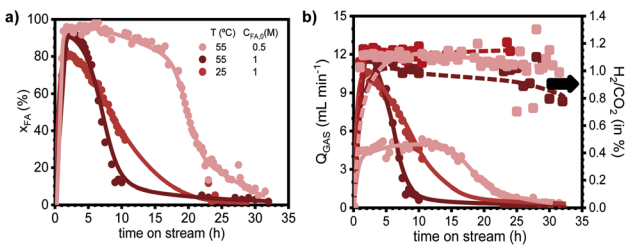

Fig. 6 (a) X_{FA} and (b) Q_{GAS} produced and H_2/CO_2 ratio in the evolved gas (%) upon time-on-stream under different operating conditions with $\tau = 160$ g_{CAT} h L^{-1}.

Table 3 Main results obtained in the FA dehydrogenation over 3D Pd/AC catalysts under different operating conditions. Data collected from Fig. 6 and 7

Operating conditions	Cycles	$X_{FA\ max}$ (%)	t_{stable} (h)	$t_{operation}$ (h)	V_{GAS} (L)	V_{H_2} (L)	$V^*_{H_2}$ (L g_{CAT}^{-1})
T = 55 °C, $C_{FA,0}$ = 0.5 M	1st use	99	12.0	31.5	5.6	3.0	1.2
T = 55 °C, $C_{FA,0}$ = 1 M	1st use	93	3.0	23.0	4.4	2.3	1.0
	2nd use	94	3.5	22.0	3.8	2.0	1.0
	3rd use	94	1.8	11.0	1.8	0.9	0.6
	4th use	90	1.8	8.5	0.8	0.4	0.4
	5th use	83	0.5	9.0	0.3	0.2	0.3
T = 25 °C, $C_{FA,0}$ = 1 M	1st use	81	3.8	24.0	6.4	3.4	1.2
	2nd use	88	4.3	23.5	5.1	2.7	1.2
	3rd use	83	4.0	24.0	3.6	1.9	1.2
	4th use	85	2.3	18.5	1.7	0.9	0.8
	5th use	69	2.5	15.0	0.6	0.3	0.5

et al.[30] exhibited X_{FA} in the range of 82% to 100% in the temperature range of 50 °C to 100 °C, respectively, employing a pressure of 5 atm to maintain a liquid phase reaction, $C_{FA,0}$ = 0.5 M, and low spatial times, τ = 0.44 g_{CAT} h g_{FA}^{-1}. In addition, the trimetallic powdered $PtRuBiO_x$/C catalyst provided very low FA conversions of X_{FA} = 1–3%, at 60 °C, which is likely because of the very low space-times selected of 0.007 to 0.016 g_{CAT} h g_{FA}^{-1}.[41] Strikingly, the evolved H_2 was not measured in any of these studies, which is the key factor in this chemical reaction. Herein, the evolved Q_{GAS} ranged from 5 to 12 mL min^{-1} (see Fig. 6b) depending on the $C_{FA,0}$ and the reaction temperature, where the former parameter was more critical. In addition, the H_2/CO_2 ratio was slightly above 1 under all conditions, indicating the retention of CO_2 in the reaction media, either in the aqueous solution or on the Pd surface, as reported in previous works where the reaction in the common slurry reactor was carried out in discontinuous mode.[40–42]

The progressive deactivation commonly observed in Pd/AC catalysts caused by the species present in the reaction media, particularly $HCOO^-$ and CO_2,[30] also depends on the operating conditions, which in this case was mainly $C_{FA,0}$. Specifically, the catalyst activity was prolonged up to 12 h at $C_{FA,0}$ = 0.5 M, and this value decreased to 3 h at $C_{FA,0}$ = 1 M, as shown by the t_{stable} data in Table 3. A higher temperature also accelerated the deactivation, but much less than the $C_{FA,0}$. These t_{stable} values were significantly higher than those observed in the above-mentioned studies in a continuous reactor,[30,41] in which the FA conversion decreased from the beginning of the reaction in accordance with the lower amount of catalyst loaded in the reactor necessary to work under the very low space time values.

Besides, the evolved V_{GAS} and V_{H_2} resulted from the trade-off between the evolved Q_{GAS} and the duration of the catalyst activity. Under the tested operating conditions, V_{H_2} was similar in the three experiments and ranged from 2 to 3 L (Table 3). Therefore, based on the above-mentioned results, and in contrast to that reported in the literature, it is recommended to perform the reaction at 25 °C because the catalyst lifetime is long enough to offset the lower Q_{H_2} produced. Thus, the 3D Pd/AC catalysts enabled the production of CO-free hydrogen from FA as a hydrogen carrier under ambient conditions. This finding is very significant given that it supports the use of FA as an alternative to most conventional petro-LOHCs.[19,43] The ability to produce hydrogen under ambient conditions eliminates the need for high-temperature and high-pressure processes, which are typically required for petro-LOHCs and other conventional hydrogen production processes. This translates into lower energy requirements and potentially reduced infrastructure costs for hydrogen production. These advantages reinforce the use of FA as a hydrogen carrier despite its lower hydrogen content than petro-LOHCs (4.4 *vs.* ~6 wt%).

Regarding the regenerability of the 3D Pd/AC catalysts, up to five consecutive uses of the 3D Pd/AC monoliths were conducted under the following operating conditions: $C_{FA,0}$ = 1 M and T = 25 °C and 55 °C. The temporal X_{FA}, Q_{GAS} and H_2/CO_2 profiles obtained in the consecutive uses are shown in Fig. 7 and the main results presented in Table 3. Given that the number of monoliths in the bed decreased with the number of uses, the hydrogen volume per gram of catalyst ($V^*_{H_2}$) was the most appropriate variable to study the deactivation (Table 3). As can be seen, the catalyst activity could be totally recovered after the 1st use *via* dry treatment at 60 °C. This result is consistent with previous reported results using commercial AC powder.[30,40]

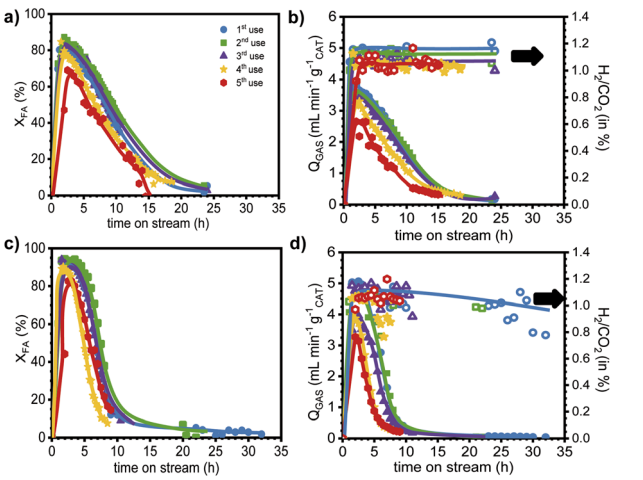

Fig. 7 (a and c) X_{FA} and (b and d) Q_{GAS} produced per gram of catalyst and H_2/CO_2 ratio in the gas flow rate (%) with time-on-stream at $C_{FA,0}$ = 1 M, τ = 160 g_{CAT} h L^{-1}, T = 25 °C (a and b) and 55 °C (c and d).

However, the activity (as $V^*_{H_2}$) began to slightly decrease after the 3rd use when the reaction was performed at 55 °C and after the 4th use at 25 °C.

To analyze in depth the causes for the deactivation of the catalyst, chemical, physical and textural characterization of the monoliths after each use was carried out (Table 2 and Fig. S3, S4 and S5,† respectively). Interestingly, the Pd particle size slightly increased after the catalytic reaction, becoming more significant as the reaction temperature increased, *i.e.*, d_P varied from 1.9 nm in the fresh 3D catalysts to 2.8 and 4.4 nm after the 5th use at 25 °C and 55 °C, respectively. Furthermore, the agglomeration of the Pd nanoparticles did not seem to affect their catalytic performance given that their particle size remained unaltered from the 3rd use (Table 2), while their activity continuously decreased (Fig. 7). In addition, a noticeable reduction in the Pd^{2+}/Pd^0 ratio was observed after the 5th use, decreasing from 1.4 in the fresh 3D Pd/AC to 0.9 at 25 °C and 0.5 at 55 °C in the tested monoliths. These results suggest that the number of active sites, which is related to the amount of electrodeficient Pd species where the $HCOO^-$ species interact,[15,43] decreased with the time-on-stream, which were not recovered after the dry recycling treatment. It should be noted that in the 3D Pd/AC catalysts employed at 25 °C, the Pd^{2+}/Pd^0 ratio began to significantly diminish after the 3rd use (Table 2) and their irreversible deactivation was observed from the 4th catalytic use. Therefore, the progressive reduction of Pd^{2+} species into Pd^0 with time-on-stream appears to be the main factor responsible for the permanent loss of activity. The agglomeration of Pd nanoparticles and the reduction of the Pd^{2+} species into Pd^0 upon reaction have previously been reported for this reaction,[15,17,30,40,44,45] although there is some controversy about their effect on the catalytic performance of monometallic Pd catalysts.

Alternatively, it was observed that S_{BET} and A_{EXT} did not diminish upon reaction and, besides, higher carbon and hydrogen contents were not observed. This fact can be explained by the presence of small molecules on the catalyst surface, such as $HCOO^-$ species and CO_2, which barely contribute to the C and H content in carbon-based catalysts.

Finally, the impact of catalyst structuration on the FA dehydrogenation reaction was studied by comparison with a control experiment conducted using the same AC support but in powder form. To achieve this, the 3D AC monoliths were crushed and ground in an agate mortar. The preparation method, involving the incorporation of Pd and its subsequent reduction was the same as that of the 3D Pd/AC catalysts, and a detailed description is provided in the ESI.† Also, the main chemical properties of the powdered Pd/AC catalyst are presented in Table S2.† The results revealed that the H_2 production was identical using both catalysts, yielding a V_{H_2} of 2.3 mL in each case (Fig. S6†). The V_{H_2} per gram of Pd was also similar, measuring 20 and 18 L g_{Pd}^{-1} in the powdered and 3D catalyst, respectively (with slight differences due to the resulting Pd load, 4.5 *vs.* 4.9 wt% in the powdered and 3D, respectively). However, some disparities were noted in the disappearance of FA, which was higher in the powdered catalyst (Fig. S6†). We attribute this behavior to the more favorable adsorption of FA on the powdered support, which is likely due to the increased available surface area, where FA remains adsorbed without undergoing further reaction.

In conclusion, the 3D Pd/AC monoliths exhibited 100% selectivity for hydrogen production in the catalytic FA dehydrogenation reaction, although they were progressively deactivated after a few uses. Besides, the 3D catalysts demonstrated exceptional activity under ambient conditions, allowing for an unprecedented hydrogen flow rate of 6 mL min^{-1} at 25 °C, 1 atm and 160 g_{CAT} h L^{-1}. The benefit of using a precise and designed flexible technique such as robocasting for manufacturing catalysts is that 3D Pd/AC catalysts can be cost-effectively produced with the desired geometry and customized to fit the reactor dimensions.

Conclusions

3D Pd/AC monolithic catalysts were additive manufactured and employed for the first time in hydrogen production *via* the dehydrogenation of FA. Self-supported 3D cellular AC architectures were robocast from pseudoplastic aqueous AC/boehmite (70/30) inks with 42 wt% solid contents, which turned after the sintering treatment into robust cellular AC/alumina scaffolds with total porosities of up to 86% and compressive strength of 0.5 MPa. The coating of the AC-based supports with 5 wt% of well-dispersed Pd nanoparticles with a size of ~2 nm and Pd^{2+}/Pd^0 ratio of 1.4 allowed the successful production of CO-free hydrogen under ambient conditions from FA. The use of the 3D Pd/AC monoliths as catalysts demonstrated the feasibility of this process. In addition, the findings suggest that FA has great potential as a hydrogen carrier due to its ability to release hydrogen under ambient conditions over 3D Pd/AC catalysts, becoming an efficient source of hydrogen and offering advantages in terms of safety, handling, and environmental impact compared to traditional petro-LOHCs.

Author contributions

Irene Diaz-Herrezuelo: investigation, methodology, writing – original draft. Gonzalo Vega: data curation, formal analysis, investigation, methodology, writing – original draft. Marina Navarro: data curation, formal analysis, investigation, methodology, writing – original draft. Pilar Miranzo: validation, writing – original draft. M. Isabel Osendi: validation, writing – original draft. Jose A. Casas: formal analysis, validation, writing – original draft. Asuncion Quintanilla: conceptualization, data curation, formal analysis, funding acquisition, investigation, methodology, supervision, validation, writing – original draft, writing – review and editing. Manuel Belmonte: conceptualization, data curation, formal analysis, funding acquisition, investigation, methodology, supervision, validation, writing – original draft, writing – review and editing.

Conflicts of interest

There are no conflicts to declare.

Acknowledgements

This work was supported by the Grants PID2021-125427OB-I00 and TED2021-130312B-I00 funded by MICIN/AEI/10.13039/501100011033 and by "ERDF A way of making Europe", and by the Grant EIN2020-112153 funded by MCIN/AEI/10.13039/501100011033 and by "European Union NextGenerationEU/PRTR". G. Vega acknowledges the Universidad Autónoma de Madrid for the Predoctoral contract. M. Navarro acknowledges the Community of Madrid for her contract under the "Programa Investigo".

References

1 O. H. Laguna, P. F. Lietor, F. J. I. Godino and F. A. Corpas-Iglesias, *Mater. Des.*, 2021, **208**, 109927.
2 R. C. Bansal and M. Goyal, *Activated Carbon Adsorption*, Taylor & Francis, CRC Group, New York, 2005.
3 M. Iwanow, T. Gärtner, V. Sieber and B. König, *Beilstein J. Org. Chem.*, 2020, **16**, 1188.
4 H. Steldinger, A. Esposito, K. Brunnengräber, J. Gläsel and B. J. M. Etzold, *Adv. Sci.*, 2019, **6**, 1901340.
5 P. Blyweert, V. Nicolas, J. Macutkevic, V. Fierro and A. Celzard, *ACS Sustainable Chem. Eng.*, 2022, **10**, 7702.
6 S. Chandrasekaran, B. Yao, T. Liu, W. Xiao, Y. Song, F. Qian, C. Zhu, E. B. Duoss, C. M. Spadaccini, Y. Li and M. A. Worsley, *Mater. Horiz.*, 2018, **5**, 1166.
7 R. Llamas-Unzueta, J. A. Menendez, M. Suarez, A. Fernandez and M. A. Montes-Moran, *Addit. Manuf.*, 2022, **59**, 103083.
8 M. J. Regufe, A. F. P. Ferreira, J. M. Loureiro, A. Rodrigues and A. M. Ribeiro, *Microporous Mesoporous Mater.*, 2019, **278**, 403.
9 A. Pereira, A. F. P. Ferreira, A. Rodrigues, A. M. Ribeiro and M. J. Regufe, *Chem. Eng. J.*, 2022, **450**, 138197.
10 D. N. D. L. Mendes, A. Gaspar, I. Ferreira, J. P. B. Mota and R. P. P. L. Ribeiro, *Chem. Eng. Res. Des.*, 2021, **174**, 442.
11 B. Verougstraete, M. Schoukens, B. Sutens b, N. V. Haute, Y. De Vos, M. Rombouts and J. F. M. Denayer, *Sep. Purif. Technol.*, 2022, **299**, 121660.
12 J. F. Rangel-Sequeda, M. Loredo-Cancino, V. I. A. Mate, D. A. de Haro-del Rio and N. E. Davila-Guzman, *Mater. Today Commun.*, 2022, **33**, 104758.
13 J. D. Acuña-Bedoya, J. F. Rangel-Sequeda, M. Loredo-Cancino, M. L. Maya-Treviño, L. P. Domínguez-Jaimes and J. M. Hernández-López, *J. Environ. Chem. Eng.*, 2022, **10**, 108203.
14 C. Chu, K. Wu, B. Luo, Q. Cao and H. Zhang, *Carbon Resour. Convers.*, 2023, **6**, 334.
15 F. Sanchez, D. Motta, A. Roldan, C. Hammond, A. Villa and N. Dimitratos, *Top. Catal.*, 2018, **61**, 254.
16 J. Eppinger and K. Huang, *ACS Energy Lett.*, 2017, **2**, 188.
17 L. Zhang, W. Wu, Z. Jiang and T. Fang, *Chem. Pap.*, 2018, **72**, 2121.
18 J. Zheng, H. Zhou, C. Wang, E. Ye, J. W. Xu, X. J. Loh and Z. Li, *Energy Storage Mater.*, 2021, **35**, 695.
19 M. Ichikawa, Organic liquid carriers for hydrogen storage, in *Solid-State Hydrogen Storage: Material and Chemistry*, ed. G. Walker, Woodhead Publishing Limited, Cambridge, England, 2008, pp. 500–532.
20 J. Y. Cho, H. Kim, J. E. Oh and B. Y. Park, *Catal*, 2021, **11**, 1497.
21 X. Shao, X. Miao, X. Yu, W. Wang and X. Ji, *RSC Adv.*, 2020, **10**, 9414.
22 S. Jiang, J. Sun, S. Zhai, T. Yu, L. Sun, L. Yang, D. Zhai, C. Liu, Z. Li, G. Ren and W. Deng, *Cell Rep. Phys. Sci.*, 2023, **4**, 101248.
23 Z. Chen, C. A. M. Stein, R. Qu, N. Rockstroh, S. Bartling, J. Weiß, C. Kubis, K. Junge, H. Junge and M. Beller, *ACS Catal.*, 2023, **13**, 4835.
24 K. Tedsree, T. Li, S. Jones, C. W. A. Chan, K. M. K. Yu, P. A. J. Bagot, E. A. Marquis, G. D. W. Smith and S. C. E. Tsang, *Nat. Nanotechnol.*, 2011, **6**, 302.
25 C. Hu, J. K. Pulleri, S. W. Tiang and K. Y. Chan, *Int. J. Hydrogen Energy*, 2014, **39**, 381.
26 W. Zhou, M. Li, O. L. Ding, S. H. Chan, L. Zhang and Y. Xue, *Int. J. Hydrogen Energy*, 2014, **39**, 6433.
27 J. Li, W. Chen, H. Zhao, X. Zheng, L. Wu, H. Pan, J. Zhu, Y. Chen and J. Lu, *J. Catal.*, 2017, **352**, 371.
28 H. Xhong, M. Iguchi, M. Chatterjee, Y. Himeda, Q. Xu and H. Kawanami, *Adv. Sustainable Syst.*, 2018, **2**, 1700161.
29 L. Di, J. Zhang, C. Ma, X. Tu and X. Zhang, *Catal. Today*, 2019, **337**, 201.
30 M. Caiti, D. Padvan and C. Hammond, *ACS Catal.*, 2019, **9**, 9188.
31 I. Barlocco, S. Bellomi, J. J. Delgado, X. Chen, L. Prati, N. Dimitratos, A. Roldan and A. Villa, *Catal. Today*, 2021, **382**, 61.
32 C. Ramírez, M. Belmonte, P. Miranzo and M. I. Osendi, *Materials*, 2021, **14**, 2111.
33 A. D. Salazar-Aguilar, A. Quintanilla, P. Lopez, C. Martinez, S. M. Vega-Díaz, J. A. Casas, P. Miranzo, M. I. Osendi and M. Belmonte, *ACS Appl. Mater. Interfaces*, 2022, **14**, 920.
34 A. C. V. Coelho, G. A. Rocha, P. S. Santos, H. S. Santos and P. K. Kiyohara, *Materia*, 2008, **13**, 329.
35 S. Penner, D. Wang, B. Jenewein, H. Gasbach, B. Klötzer, A. Knop-Gerike, R. Schölgl and K. Hayek, *J. Chem. Phys.*, 2006, **125**, 094703.
36 G. C. Cabilla, A. L. Bonivardi and M. A. Baltanás, *Appl. Catal., A*, 2003, **255**, 181.
37 M. Navlani-García, D. Salinas-Torres and D. Cazorla-Amorós, *Energies*, 2019, **12**, 4027.
38 J. Yu and P. E. Savage, *Ind. Eng. Chem. Res.*, 1998, **37**, 2.
39 C. D. Wagner, W. M. Riggs, L. E. Davis, J. F. Moulder and G. E. Muilenberg, *Handbook of X-Ray Photoelectron Spectroscopy*, Perkin-Elmer Corporation, 1979.
40 C. Martin, A. Quintanilla, G. Vega and J. A. Casas, *Appl. Catal., B*, 2022, **317**, 121802.
41 C. Hu, S. W. Ting, J. Tsui and K. Y. Chan, *Int. J. Hydrogen Energy*, 2012, **37**, 6372.
42 J. L Santos, E. R. López, S. Ivanova, A. Monzón, M. A. Centeno and J. A. Odriozola, *Chem. Eng. J.*, 2023, **455**, 140645.
43 Y. Kwak, J. Kirk, S. Moon, T. Ohm, Y. J. Lee, M. Jang, L. H. Park, C. Ahn, H. Jeong, H. Sohn, S. W. Nam, C. W. Yoon, Y. S. Jo and Y. Kim, *Energy Convers. Manage.*, 2021, **239**, 114124.
44 H. Jeon and Y. Chung, *Appl. Catal., B.*, 2017, **210**, 212.
45 Y. Kim and D. H. Kim, *Appl. Catal., B*, 2019, **244**, 684.